Nature Communications

https://doi.org/10.1038/s41467-026-73117-w

Article in Press

Gauge-field-induced duality group in metamaterials

Received: 25 September 2025

Accepted: 1 May 2026

Cite this article as: Meng, Y., Zou, H.-y., Zheng, N. *et al.* Gauge-field-induced duality group in metamaterials. *Nat Commun* (2026). https://doi.org/10.1038/s41467-026-73117-w

Yan Meng, Hong-yu Zou, Naifu Zheng, Linyun Yang, Ruo-Yang Zhang, Jingming Chen, Xiang Xi, Bei Yan, Yong Ge, Yi-jun Guan, Hong-xiang Sun, Gui-Geng Liu, Zhenxiao Zhu, Shou-qi Yuan, Ce Shang, Hongsheng Chen, Qihang Liu, Yihao Yang & Zhen Gao

Gauge-field-induced duality group in metamaterials

Yan Meng[1,2,3,4,5†], Hong-yu Zou[6†], Naifu Zheng[7,8†], Linyun Yang[3,4,5†], Ruo-Yang Zhang[9,10], Jingming Chen[3,4,5], Xiang Xi[2,3,4,5], Bei Yan[3,4,5], Yong Ge[6], Yi-jun Guan[6], Hong-xiang Sun[6], Gui-Geng Liu[11], Zhenxiao Zhu[12*], Shou-qi Yuan[6*], Ce Shang[13], Hongsheng Chen[14,15], Qihang Liu[7,8*], Yihao Yang[14,15*], Zhen Gao[3,4,5*]

[1]Marine Science and Technology Domain, Beijing Institute of Technology, Zhuhai 519088, China.
[2]School of Electrical Engineering and Intelligentization, Dongguan University of Technology, Dongguan, 523808, China
[3]State Key Laboratory of Optical Fiber and Cable Manufacturing Technology, Southern University of Science and Technology, Shenzhen 518055, China.
[4]Department of Electronic and Electrical Engineering, Southern University of Science and Technology, Shenzhen 518055, China.
[5]Guangdong Key Laboratory of Integrated Optoelectronics Intellisense, Southern University of Science and Technology, Shenzhen 518055, China.
[6]Research Center of Fluid Machinery Engineering and Technology, School of Physics and Electronic Engineering, Jiangsu University, Zhenjiang 212013, China.
[7]Department of Physics, Southern University of Science and Technology, Shenzhen 518055, China.
[8]State Key laboratory of quantum functional materials, Southern University of Science and Technology, Shenzhen 518055, China.
[9]National Laboratory of Solid State Microstructures, School of Physics, Nanjing University, Nanjing 210093, China.
[10]Collaborative Innovation Center of Advanced Microstructures, Nanjing 210093, China.
[11]Department of Electronic and Information Engineering, School of Engineering, Westlake University, Hangzhou, 310030, China.
[12]Frontier Interdisciplinary Domain, Beijing Institute of Technology, Zhuhai 519088, China.
[13]Aerospace Information Research Institute, Chinese Academy of Sciences, Beijing 100094, China.
[14]Interdisciplinary Center for Quantum Information, State Key Laboratory of Modern Optical Instrumentation, College of Information Science and Electronic Engineering, Zhejiang University, Hangzhou 310027, China.
[15]ZJU-Hangzhou Global Science and Technology Innovation Center, Key Laboratory of Advanced Micro/Nano Electronic Devices and Smart Systems of Zhejiang, ZJU-UIUC Institute, Zhejiang University, Hangzhou 310027, China.

[†]These authors contributed equally to this work.
*Corresponding author. Email: zhuzhenxiao@bitzh.edu.cn (Z.Z.); shouqiy@ujs.edu.cn (S.Q.Y.); liuqh@sustech.edu.cn (Q.L.); yangyihao@zju.edu.cn (Y.Y.); gaoz@sustech.edu.cn (Z.G.)

Dualities are mappings that connect seemingly unrelated physical systems, enabling simplification and reinterpretation via duality transformations. However, prior studies have been predominantly limited to one-to-one mappings isomorphic to a $\mathbb{Z}_2$ group, where self-duality occurs only at a single point at which the lattice maps onto itself under a duality transformation. Here, we extend the duality framework by incorporating gauge fields that modify symmetry representations, constructing more general duality groups, $\mathbb{Z}_2 \times \mathbb{Z}_2$ in two-dimensional systems and $(\mathbb{Z}_2)^6$ in three-dimensional systems. We theoretically establish and experimentally validate that such gauge-field-induced duality groups link multiple distinct metamaterials across different symmetry classifications while sharing identical band structures. Notably, in three-dimensional systems, gauge fields promote self-duality from a single point to a set, yielding fourfold degeneracies across the entire Brillouin zone and an eightfold-degenerate double Dirac point. Our work expands duality research and deepens the understanding of hidden symmetries in complex physical systems.

Introduction

As a form of hidden symmetry [1–4], duality [5] is ubiquitous across diverse systems, manifesting as discrete or continuous, global or local symmetries. It uncovers intrinsic mathematical mappings between distinct physical systems, offering a pathway to transform problems in complex systems that are challenging for theoretical analysis or experimental verification into simpler systems [6]. Representative examples include duality between the quantum gravity in an Anti-de Sitter spacetime and the conformal field theory on its lower-dimensional boundary [7,8], the Ising model [9], and electromagnetic duality between electric and magnetic fields in Maxwell's equations [10], which underpins both the topological insulators [11,12] and conformal transformation optics [13–15]. More recently, duality transformations within a single system across different structural parameters have been discovered in mechanics [16–17], exhibiting identical elasticity and band structure across distinct structural configurations [18–21]. It is found that at a critical point termed self-duality, configurations remain invariant under duality transformations and exhibit distinct properties, such as extra degeneracies protected by these hidden symmetries [16–21], isotropic elasticity without the requirement of spatial symmetries [17], and the emergence of fragile and higher-order topological phases [21] in mechanics.

Duality groups comprise transformations that relate distinct Hamiltonians through parameter-space mappings combined with linear (or antilinear) operations on the Hilbert space. In certain parameter configurations, these transformations leave the Hamiltonian invariant and are realized as emergent symmetries, defining what we refer to as self-dual configurations. Such dualities arise either from explicit construction using representation theory or from hidden structural constraints imposed by system design and physical equivalences. Unlike isolated $\mathbb{Z}_2$-type dualities between two configurations, a full duality group organizes an entire family of Hamiltonians into a symmetry-related multiplet, revealing deeper algebraic and geometric structures underlying the parameter space. To date, however, most prominent examples of duality phenomena consist of two distinct configurations [1–21], corresponding to the simplest $\mathbb{Z}_2$ duality group. More complex duality phenomena and the associated structure of duality groups have been rarely studied.

In this work, we extend the duality framework from the $\mathbb{Z}_2$ group to $\mathbb{Z}_2 \times \mathbb{Z}_2$ in two-dimensional (2D) systems and $(\mathbb{Z}_2)^6$ in three-dimensional (3D) systems by incorporating artificial gauge fields, which are engineered by designing positive and negative couplings with gauge degrees of freedom (DOFs) and have emerged as a powerful tool for enriching symmetry group representations and realizing exotic topological phases [22–36]. We theoretically establish that, mediated by duality transformations, multiple lattices within a group can exhibit identical gauge fluxes and band structures despite distinct configurations and symmetry classifications. Under our design of artificial gauge fields, we realize two duality groups with Abelian *p*-group structures, a 2-group of order 4 ($\mathbb{Z}_2 \times \mathbb{Z}_2$) in 2D and a 2-group of order 64 ($(\mathbb{Z}_2)^6$) in 3D systems. In addition, self-dual lattices that remain invariant under duality transformations are protected by a duality symmetry and give rise to extra degeneracies, including Kramers-like twofold (fourfold) degeneracy across the entire Brillouin zone (BZ) in 2D (3D) systems. Furthermore, we experimentally verify that distinct 2D acoustic metamaterials with 0-gauge flux, connected by duality transformations within a $\mathbb{Z}_2 \times \mathbb{Z}_2$ duality group, share identical band structures. Notably, the self-dual 2D acoustic metamaterial with a π gauge flux exhibits a doubly degenerate band structure across the entire BZ. In 3D acoustic metamaterials, the enhanced DOFs from spatial dimensionality and gauge fields result in one duality configuration set and three self-duality configuration sets, all interconnected via duality transformations forming a $(\mathbb{Z}_2)^6$ duality group. Among them, the self-duality configurations with 2π and 4π gauge fluxes exhibit doubly degenerate bands, while the configuration with 6π gauge flux exhibits fourfold degeneracy across the entire BZ and an eightfold degenerate double Dirac point.

Results

Duality in 2D lattices

We initiate our exploration of dual and self-dual mechanisms at the Hamiltonian level. The Hamiltonian of duality lattices incorporating artificial gauge fields can be expressed within the tight-binding model [6]:

$$\hat{H} = \sum_{\langle m,n\rangle} t_{mn} s_m^{\dagger} s_n \,, \tag{1}$$

where $\langle m, n\rangle$ denote all nearest-neighbor pairs, and $s_m^{\dagger}$ (s_n) is the creation (annihilation) operator at site *m* (*n*). The hopping parameter t_{mn} characterizes the coupling between sites *m* and *n* and is taken to be real in this work. Its sign encodes the specific coupling configuration of the lattice, allowing for both positive and negative hopping amplitudes and thereby enabling the implementation of artificial gauge fields. For simplicity and without loss of generality, we choose the absolute values of all nonzero hopping amplitudes to be equal throughout the lattice. As illustrated in Fig. 1a, a parameter p_i in a smooth parameter space can be mapped onto p_j $(j \neq i)$ via the function f_i. Similarly, the Hamiltonian $\hat{H}(p_i)$, can be transformed into $\hat{H}(p_j)$ by a dual operator $\hat{D}_i$, following the relation $\hat{H}(p_2) = \hat{D}_1\hat{H}(p_1)\hat{D}_1^{\dagger} = \hat{D}_2\hat{H}\,(p_3)\hat{D}_2^{\dagger}$. This implies that any Hamiltonian within one group can be mapped onto another via the dual operators $\hat{D}_i$. In principle, the Hamiltonian can be realized in atomic orbital, mechanical, photonic, and acoustic systems, provided the coupled-mode model is applicable [37,38].

We consider two lattice configurations to be "equivalent" if they are related either by the point-group symmetry operations in G_p, or by a global sign-flip redundancy represented by the group G_0. The latter acts by inverting all coupling signs, such that for any representative Hamiltonian $\hat{H}(t_{mn})$, the transformed Hamiltonian satisfies $\eta\hat{H}(t_{mn})\eta^{\dagger} = \hat{H}(-t_{mn}) = -\hat{H}(t_{mn})$, where $\eta \in G_0$. The full symmetry group is given by the direct product $G = G_p \times G_0$, which acts on the configuration space *X* consisting of all lattice configurations under consideration. The number of symmetry-inequivalent lattices, corresponding to the orbits of *X* under the action of *G*, can be determined using Burnside's lemma [39]:

$$N = |X/G| = \frac{1}{|G|}\sum_{g\in G}|X_g| \tag{2}$$

where $X_g = \{\xi \in X | g \circ \xi = \xi\}$ represents lattices invariant under g and $|G|$ denotes the order of the group.

For the 2D square lattices shown in Fig. 1b, the spatial symmetry group is $G_p = D_{4h}$. The global sign-flip symmetry is described by $G_0 = \{\mathbb{I}_4, \eta_{2D}\}$, with $\eta_{2D} = \mathrm{diag}(1, -1, -1, 1)$. This leads to the full symmetry group $G_{2D} = D_{4h} \times G_0$ with $|G_{2D}| = 32$, from which we obtain $N_{2D} = 4$ symmetry-inequivalent lattice configurations (one self-dual lattice and three dual lattices). Without loss of generality, we select one representative lattice from each equivalent lattice set to illustrate multi-to-multi mappings between lattices within the duality group. The gauge flux Φ, defined via $\exp(i\Phi) = \prod_{\langle m,n \rangle} \mathrm{sign}\,(t_{mn})$ [22] as the accumulated sign of coupling bonds around each plaquette, takes quantized values of 0 or π. The duality transformations between lattices within the duality group are represented by curved arrows and denoted as $\widehat{D}_i$ (i = 1, 2, 3), as shown in Fig. 1b, which consist of a local gauge transformation $\widehat{U}_i$, a spatial inversion operation $\widehat{P}$, and the time-reversal symmetry operator $\widehat{\Theta}$, such that $\widehat{D}_i = \widehat{U}_i \widehat{P} \widehat{\Theta}$. The selection of $\widehat{U}_i$ is not irreplaceable. Here, we adopt the simplest diagonal unitary operators: $\widehat{U}_1 = \mathrm{diag}(1, -1, 1, -1)$, $\widehat{U}_2 = \mathrm{diag}(1, 1, -1, 1)$, and $\widehat{U}_3 = \widehat{U}_1 \circ \widehat{U}_2 = \mathrm{diag}(1, -1, -1, -1)$. Together with the identity $\widehat{U}_0 = \hat{\mathbb{I}}_4$, the set of operators $\{\widehat{U}_i\}$ forms a $\mathbb{Z}_2 \times \mathbb{Z}_2$ duality group, which is an Abelian 2-group with 4 group elements.

In contrast to conventional space groups, this gauge-induced group constrains the sign of coupling tubes, protects degeneracies via internal parity configurations, and enables duality relations between geometrically distinct but physically equivalent lattices. The effects of these gauge transformation operators on dual and self-dual lattices are illustrated in Fig. 1c and 1d, respectively. The $\pm$ sign at each lattice site represents localized gauge freedoms: a gauge transformation inverts the signs of a coupling bond t_{mn} if the signs at sites *m* and *n* are opposite. Fig. 1c depicts a transformation sequence from lattice ① to lattice ②, then to lattice ③, and finally back to lattice ①, demonstrating the Abelian 2-group structure. In contrast, Fig. 1d shows that the self-dual lattice ④ remains equivalent (connected by operations in G) under all duality transformation operators, highlighting its critical and unique role in the duality.

For spatially 2D periodic lattices, the momentum-space representation of the Hamiltonian provides a convenient framework and can be written as:

$$\widehat{H}_{\mathrm{2D}} = \sigma_\lambda \otimes M_x + M_y \otimes \sigma_\lambda, \tag{3}$$

where σ_λ denotes the Pauli matrix with $\lambda = 0, 3$, and the Kronecker products encode the tensor-product structure of the Hilbert space associated with the lattice degrees of freedom along the *x* and *y* directions. Each σ_λ represents a two-level subspace that remains unaffected by the hopping process along the orthogonal direction. The matrices M_α $(\alpha = x, y)$ take the identical form $M_\alpha = \begin{pmatrix} 0 & u_\alpha^* \\ u_\alpha & 0 \end{pmatrix}$, with $u_\alpha = t_{mn}(1 + e^{ik_\alpha})$ being the Bloch functions along k_α.

To illustrate the mapping between Hamiltonians of different lattices, we take lattice ① and lattice ② in Fig. 1b as an example. First, applying the combined gauge transformation $\widehat{U}_1$ and spatial inversion operation $\hat{P}$ to the Hamiltonian of lattice ① ($\widehat{H}_{2D}^1$), yields:

$$\left(\widehat{U}_1\hat{P}\right)\widehat{H}_{2D}^1(t_x, \mathbf{k})\left(\widehat{U}_1\hat{P}\right)^\dagger = \widehat{H}_{2D}^1(-t_x, -\mathbf{k}). \tag{4}$$

where $t_x = t_{12} = t_{34}$ for lattice ①. Here, $\widehat{U}_1$ solely changes the sign of hopping amplitudes along the *x* direction, while $\hat{P}$ enforces wavevector inversion from $\mathbf{k}$ to $-\mathbf{k}$. Second, the time-reversal operator $\widehat{\Theta}$ further satisfies $\widehat{\Theta}\widehat{H}_{2D}^1(t_x, -\mathbf{k})\widehat{\Theta}^\dagger = \widehat{H}_{2D}^1(t_x, \mathbf{k})$. The combination $\widehat{D}_1 = \widehat{U}_1\hat{P}\widehat{\Theta}$ defines an antiunitary operator with $\widehat{D}_1^2 = -\mathbb{I}_4$, leading to the duality mapping:

$$\widehat{D}_1\widehat{H}_{2D}^1(t_x, \mathbf{k})\widehat{D}_1{}^\dagger = \widehat{H}_{2D}^1(-t_x, \mathbf{k}) = \widehat{H}_{2D}^2(t_x, \mathbf{k}). \tag{5}$$

Thus, the Hamiltonians of lattice ① and lattice ② ($\widehat{H}_{2D}^1$ and $\widehat{H}_{2D}^2$) are dual to each other via the duality operator $\widehat{D}_1$. As exemplified in Fig. 1d, the self-duality lattice ④ is invariant under all duality operators $\widehat{D}_i$, such that $\widehat{D}_i\widehat{H}_{2D}^4\widehat{D}_i{}^\dagger = g\widehat{H}_{2D}^4 g^\dagger$, which again indicates that duality acts as a symmetry of the self-duality lattice. Notably, the lattices with 0 gauge flux in the 2D system construct a duality group, exhibiting richer multiple-to-multiple mappings compared to the one-to-one mappings in conventional systems [16–20,37] and one-dimensional (1D) cases (see Note 1 and Note 2 in Supplementary Information). Whereas the duality group in Ref. [38] is the cyclic group C_3 generated by a single duality operator, our framework generalizes this structure by incorporating three distinct duality operators, forming a $\mathbb{Z}_2 \times \mathbb{Z}_2$ duality group.

Experimental observation of the duality group in 2D acoustic metamaterials

To experimentally validate the duality group and self-duality in 2D systems, we design and fabricate three acoustic metamaterial samples, as shown in Fig. 2a-c. The unit cell of each sample is outlined by a red dashed box and enlarged in the upper right inset. Each unit cell comprises four cuboid cavities, and two neighboring cavities are connected by an air tube, which serves as the coupling between sites in the tight-binding model illustrated in the lower-left inset. The sign of the coupling is determined by the connectivity of coupling tubes, which is characterized by the geometric parameter Δd. Specifically, the couplings along the *x* direction (t_{12}, t_{34}) are all positive (negative) for $\Delta d > 0$ ($\Delta d < 0$), while the couplings possess opposite signs ($t_{12} = -t_{34}$) for

$\Delta d = 0$ (see Note 3 in Supplementary Information).

The experimentally measured band structures, extracted from the Fourier transform of the spatial distributions of complex acoustic pressures, are plotted as color maps in Fig. 2d-f. It can be seen that the measured bulk band structures of the two dual acoustic metamaterials with 0-gauge flux (Fig. 2d, f) are identical, despite their different structural configurations, thereby verifying their duality relation. To compare with the experimental results, analytical band structures derived from Eq. (3) are presented as solid lines, where a uniform frequency offset of 4310 Hz is manually added to all bands in post-processing to align the theoretical spectra with the 2D resonance frequency of the acoustic resonators. Such a uniform shift does not affect the band topology, degeneracy structure, or duality relations discussed in this work. The coupling strengths are taken as $t_{mn} = \pm 30$ Hz, extracted from the commercial software (COMSOL Multiphysics). The good agreement between the experimental and analytical results not only validates the accuracy of the tight-binding approximation and the experimental measurements but also confirms the effectiveness of the strategy for constructing dual acoustic metamaterials with artificial gauge fluxes.

The measured bulk band structure of the self-dual metamaterials (Fig. 2b) is shown in Fig. 2e, which exhibits a Kramers-like double degeneracy across the entire BZ, arising from the self-duality symmetry enforced by the antiunitary operator $\widehat{D}$. In contrast to the 0-gauge flux case, in the π-gauge flux metamaterial, the duality operation $\widehat{D}$ itself becomes a symmetry operation ($\widehat{D}_i^2 = -1$), thereby guaranteeing a Kramers-like degeneracy (see Note 4 in Supplementary Information). A fourfold degenerate Dirac point appears at the *M* point, which is protected by the artificial gauge fields rather than the conventional point group symmetry [33,40]. Furthermore, the duality mappings between acoustic metamaterials with different configurations are schematically illustrated in Fig. 2g. Metamaterials with opposite Δd values are related by a dual operator, while metamaterials with $\Delta d = 0$ remain invariant under the same dual transformation (see Supplementary Note 5 and Supplementary Movie 1).

Duality groups and self-duality groups in 3D systems

We now extend the concepts of duality and self-duality from 2D to 3D systems. To explore these concepts, we consider a $\mathbb{Z}_2$ 3D gauge model defined on a cubic lattice comprising eight sites per unit cell, as illustrated in Fig. 3a(i)-(iv). The total gauge flux of a 3D unit cell is defined as the cumulative flux across all six plaquettes on its surfaces: $\Phi_{3\mathrm{D}} = \sum_{q=1}^{6} \Phi_q$, where q indexes each plaquette [41]. Based on this definition, the cubic lattice can be classified into four distinct categories characterized by total gauge fluxes of 0, 2π, 4π, and 6π, respectively. According to Burnside's lemma [39], the duality group with 0-gauge flux contains 8 inequivalent lattice configurations, while the self-duality groups with 2π, 4π, and 6π-gauge flux consist of 9, 11, and 4 inequivalent lattices, respectively.

Benefiting from the higher dimensionality and the increased number of local DOFs in 3D systems, the self-duality groups feature enriched multi-to-multi mappings rather than a single self-dual point in 2D systems (see Note 6 in Supplementary Information). As illustrated in Fig. 3b(i), two representative lattices with 0-gauge flux belonging to the duality group in Fig. 3a(i) are related by a gauge transformation operator $\widehat{U}_4 = \sigma_3 \otimes \sigma_0 \otimes \sigma_3$. All lattices in the self-duality groups with 2π, 4π, and 6π-gauge flux remain invariant under $\widehat{U}_4$, as illustrated in Fig. 3b(ii)-(iv), respectively. Furthermore, the inequivalent lattices within the self-duality group with 6π-gauge flux remain invariant under all gauge transformations belonging to the 2π and 4π self-duality groups, revealing a hierarchical structure unique to 3D systems (see Note 7 in Supplementary Information).

To elucidate the operator origin of these multi-to-multi lattice mappings, we now analyze the structure of the duality operators themselves. Each duality operator $\widehat{D}_{3\mathrm{D}}$ connecting dual lattices [blue arrows in Fig. 3a(i)-(iv)] is expressed as $\widehat{D}_{3\mathrm{D}} = \widehat{U}_{3\mathrm{D}}\widehat{P}\widehat{\Theta}$, where $\widehat{U}_{3\mathrm{D}}$ is a unitary gauge transformation acting on the local DOFs, $\widehat{P}$ denotes a spatial inversion operation, and $\widehat{\Theta}$ is the time-reversal symmetry operator. To characterize the gauge sector, we first enumerate all admissible unitary gauge operators $\{\widehat{U}_i\}$ compatible with the symmetry constraints of the 3D cubic lattice. Each $\widehat{U}_i$ acts diagonally on the 8-site basis with eigenvalues ± 1, leading to $2^8 = 256$ candidate local sign-flip configurations. After eliminating redundancies associated with the global sign-flip symmetry $G_0 = \{\mathbb{I}_8, \eta_{3D}\}$, where $\eta_{3D} = \mathrm{diag}(1, -1, -1, 1, -1, 1, 1, -1)$, as well as the space-group symmetries G_p, the configurations reduce to 64 inequivalent gauge-operator classes. The resulting set of gauge transformations is closed under composition and forms an Abelian group isomorphic to $(\mathbb{Z}_2)^6$. Despite this simple Abelian algebraic structure, the physical realization in the 2π, 4π, and 6π flux self-dual groups is intrinsically nontrivial [31]. The duality operators form a projective antiunitary realization characterized by the discrete relation $D^2 = -\mathbb{I}_8$, which cannot be removed by any gauge choice. This relation leads to universal degeneracies across the entire Brillouin zone, which will become explicit in the band analysis below.

The Hamiltonian of the 3D cubic lattices can be written as:

$$\widehat{H}_{3\mathrm{D}} = \sigma_\lambda \otimes \sigma_\lambda \otimes M_x + \sigma_\lambda \otimes M_y \otimes \sigma_\lambda + M_z \otimes \sigma_\lambda \otimes \sigma_\lambda, \quad (6)$$

where M_z takes the same form as M_x and M_y in the 2D case and σ_λ denotes the Pauli matrix with $\lambda = 0, 3$. The Kronecker products explicitly encode the tensor-product structure of the Hilbert space associated with the three orthogonal lattice directions (x, y, z). The band structures extracted from Eq. (6) with $t_{mn} = \pm 72$ Hz are shown in Fig. 3c(i)-(iv), where a uniform frequency offset of 7080 Hz is added to all eigenfrequencies in post-processing to match the onsite resonance frequency of the 3D acoustic resonators. Such a global shift does not affect the band structure or degeneracy structure, but merely fixes the reference frequency.

For the cubic lattice realized with uniformly negative couplings, which corresponds to a zero gauge flux ($\Phi = 0$) under our gauge convention, the band structure exhibits an eightfold degeneracy at the *R* point. This degeneracy arises from the cubic symmetry group O_h combined with band folding induced by the enlarged unit cell along all three directions. Akin to the 2D case, self-dual lattice groups with $\Phi = 2\pi$ and $\Phi = 4\pi$ exhibit doubly degenerate band structures across the entire 3D BZ, which are protected by the duality symmetry. In addition, the self-duality group with 6π-gauge flux enforces fourfold degeneracies across the entire 3D BZ, including an eightfold degenerate double Dirac cone at the *R* point (see Note 8 in Supplementary Information). These universal degeneracies differ from accidental ones, which occur only at isolated points and require finely tuned parameters. In contrast, duality-enforced degeneracies arise from the projective representation structure of the antiunitary duality operator and remain robust under all perturbations that preserve the duality. As a result, the associated degeneracy is symmetry-protected throughout the entire Brillouin zone and is not an accidental consequence of commuting operations or fine-tuned parameters.

Based on the tight-binding configurations, we design and fabricate three 3D acoustic metamaterials: two with 0-gauge flux but different configurations and one with 6π-gauge flux, as shown in Fig. 4a-c. Each unit cell (whose top view is highlighted by a green rectangle in the lower-right insets) comprises eight cuboid cavities connected by positive or negative coupling tubes (see Note 9 in Supplementary Information). The measured bulk band structures (color maps) of the two dual metamaterials (Fig. 4d, f) exhibit excellent agreement, confirming their duality relation. For the self-dual metamaterial, the measured bulk band structure (Fig. 4e) reveals a fourfold degeneracy across the entire 3D BZ and a double Dirac point at the *R* point. The modal projection indicates that the contributions of the four degenerate eigenmodes are approximately equal, with weights close to 1/4 (see Methods and Note 10 in the Supplementary Information). To further highlight the feature of the double Dirac point, we plot the measured 3D band structures as functions of k_x, k_y, and k_z at fixed values $k_z = \pi$, $k_x = \pi$, and $k_y = \pi$, respectively. Dirac-cone dispersions are observed along all three orthogonal momentum cuts near the band-crossing frequency of approximately 7.08 kHz. The corresponding iso-frequency contour surfaces, extracted at $f =$ 6.98, 7.03, 7.08, 7.13, and 7.18 kHz, are shown in the right panel of Fig. 4g. The near-spherical symmetry of these contours in momentum space confirms the presence of a Dirac-like cone structure in all three orthogonal **k**-directions, which has remained experimentally challenging to observed since its discovery in 2016 based on space group theory [43].

Discussion

In conclusion, we have theoretically established and experimentally demonstrated the extension of duality from one-to-one mappings to the duality group with multi-to-multi mappings in acoustic metamaterials with $\mathbb{Z}_2$ gauge fields. We show that structurally distinct metamaterials belonging to different symmetry classes can share identical bulk band structures, thereby revealing hidden symmetries beyond conventional space-group theory. In particular, metamaterials within the self-duality group remain invariant under duality transformations and exhibit Kramers-like twofold (fourfold) degeneracies across the entire BZ in 2D (3D) systems. Furthermore, we experimentally observe an eightfold degenerate double Dirac point (double Dirac semimetal) in acoustic metamaterials belonging to the 3D self-duality group with 6π gauge flux. Such self-dual-enforced high-degeneracy bands offer a platform-independent mechanism for realizing symmetry-protected degeneracies. This mechanism enables the controlled excitation of high-dimensional modal subspaces, supporting applications ranging from multi-channel wave control in acoustics and photonics to phenomena driven by an enhanced density of states [45], such as phononic lasing [46, 47] and efficient sound-power emission [48]. As our framework is built upon a tight-binding formalism, it can be readily generalized to other classical wave systems such as photonics, mechanics, and electrical circuits. This work advances the understanding of complex duality phenomena and their associated mathematical frameworks, thereby providing a general framework for investigating a broader range of physical phenomena.

Methods

Analytical results from the tight-binding Hamiltonian of duality lattices. For periodic structures, the band structure for all 2D and 3D duality lattices can be obtained by solving the eigenvalue problem of the system Hamiltonian as a function of the Bloch wavevector $\mathbf{k}$. In 2D systems, $\mathbf{k} = (k_x, k_y)$, while in 3D systems, $\mathbf{k} = (k_x, k_y, k_z)$. To solve the boundary states within a supercell, the Hamiltonian was truncated along the finite dimensions of the supercell while retaining periodic boundary conditions in the remaining directions. In this case, the Hamiltonian of the supercell can be expressed as the Kronecker product of the Hamiltonians of the constituent unit cells, with the total number of terms matching the number of cells along the finite direction. The obtained band structure of the supercell corresponds to the eigenvalues of this finite Hamiltonian as a function of the Bloch wavevector in the periodic direction, thereby containing both the bulk bands and boundary states. Furthermore, when the supercell is finite along all spatial directions, the system loses translational periodicity. The full Hamiltonian can then be constructed as a Kronecker product over the finite number of unit cells. Solving this Hamiltonian yields the discrete eigenfrequency spectrum of the finite structure, which may host bulk modes, boundary-localized modes, and higher-order corner states. The analytical band structures are shown in the main text and Notes 2, 8, and 9 in the Supplementary Information.

Experimental samples fabrication. The experimental samples are fabricated using a standard 3D stereolithography technique (Kings SLA 800 Pro) with the photosensitive resin as the printing material, which has a modulus of 2880 MPa and a density of 1.10 $\mathrm{g/cm^3}$. The outer surfaces of the samples are rigid and thick enough (~ 2 mm) to be regarded as sound hard boundaries that enclose a hollow air-filled region. For the 2D samples, due to the relatively small sample size, a monolithic fabrication strategy was adopted. After printing, the residual resin inside the hollow regions was first dissolved using chemical solvents, followed by mechanical cleaning to ensure a smooth inner surface. This treatment reduces frictional losses arising from surface roughness during acoustic wave propagation. In the 2D configuration with 12×12 unit cells, each unit cell incorporates four rectangular acoustic resonators, each with two pre-formed apertures for both excitation and detection. In contrast, for the 3D samples with 10×10×10 unit cells, involving multiple stacked 2D layers, monolithic fabrication is more challenging. Therefore, the samples were printed in segments, with every three layers fabricated as one part. Adjacent parts were assembled using mortise-and-tenon-like interlocking structures and further sealed with adhesive to ensure airtightness, thereby minimizing radiation losses during acoustic wave propagation.

Experimental setup and band structure measurement. The experimental measurements are performed using a standard acoustic setup. A miniature acoustic transducer (10 mm in diameter, covering 4–8 kHz) is used as the excitation source and placed at the central cavity of the sample to generate sound waves. Specifically, for the 2D acoustic sample containing 12×12 unit cells, the excitation source is placed at the lower-left sublattice site of the unit cell indexed by (6,6). For the 3D acoustic sample containing $10 \times 10 \times 10$ unit cells, the excitation source is located at the bottom-front-left sublattice site of the unit cell indexed by (5,5,5). The sublattice site is defined as the origin of each unit cell in the local Cartesian coordinate system. A probe microphone with a 3 mm radius, mounted at the tip of a stainless-steel rod, is inserted into each cavity to measure acoustic signals point by point. During the measurements, the microphone tip is positioned near the center of the cavity height and kept away from the cavity walls to minimize boundary effects and ensure reliable measurement of the local acoustic pressure. Both the source transducer and the probe microphone are connected to a vector network analyzer (Keysight E5061B), which provides the excitation signal and simultaneously records the acoustic response. Prior to the measurements, the vector network analyzer is electronically calibrated to remove the frequency-dependent responses of the cables and electronic components. An additional reference measurement is performed by directly coupling the transducer and microphone in free space, and all measured spectra are normalized to this reference to eliminate the intrinsic response of the acoustic transducers. The probe is mounted on a computer-controlled 3D stepper, enabling automated scanning of the pressure field with sub-millimeter precision. During measurements, all unused probe holes are manually sealed with rubber plugs to suppress radiation leakage. For the 2D samples, only the cavity under investigation is unplugged to allow the microphone to be inserted, while all other cavities remain sealed. In contrast, for the 3D systems, the rubber plugs are placed only on the top and bottom surfaces of the sample, with the internal channels remaining open. When measuring a specific channel, the corresponding plug is manually removed, and the microphone, mounted on the motorized stepper, is inserted from the bottom and automatically scans upward. For the 2D and 3D samples, the full spatial distribution of the acoustic response is obtained by sequentially probing all cavities of the structure. Acoustic foams are placed around the sample to suppress unwanted reflections from the environment. After the spatial data are collected, a discrete spatial Fourier transform is applied to reconstruct the dispersion relation. For the 2D samples, the transformation yields the Bloch wavevectors (k_x, k_y), while for the 3D samples it provides the full momentum components (k_x, k_y, k_z). By plotting the Fourier-transformed spectra as a function of frequency and wavevector, the experimental band structures are obtained. For clarity, the bulk bands are shown along the high-symmetry directions of the BZ.

Modal projection of experimental nearfield onto Bloch eigenmodes. To verify that the experimentally observed response at a degenerate band arises from the superposition of the computed Bloch eigenmodes, we perform the following quantitative analysis. First, the Bloch eigenmodes of a single unit cell consisting of eight sublattice sites are numerically calculated at each high-symmetry (k, ω) point to obtain the fourfold degenerate eigenmodes v_j (j = 1, …, 4). The eigenmodes are orthonormalized within the degenerate subspace to fix the gauge and ensure $\langle v_m | v_n \rangle = \delta_{mn}$. In the experiment, the complex acoustic pressure responses p_i are independently measured at each sublattice site (i = 1, …, 8) in all unit cells. After Fourier transformation, the complex Fourier-transformed spectra $A_i(k, \omega)$ are obtained. At a given wavevector (k), the peak frequency in the Fourier spectra corresponds to the eigenfrequency of the excited mode, and the complex amplitudes at this frequency are extracted for all eight sublattice sites. Collecting these amplitudes yields an eight-component complex vector $\Psi(k, \omega) = (A_1, A_2, \dots, A_8)^T \in \mathbb{C}^8$, which represents the experimentally measured eigenmode of a single unit cell. The experimentally measured eigenmode Ψ is then projected onto the orthonormal basis of the simulated degenerate eigenmodes via $c_j = \langle v_j | \Psi \rangle$, and the relative modal contribution of each eigenmode j is quantified by $w_j = |c_j|^2 / \sum_{m=1}^{4} |c_m|^2$. To further reduce the possible excitation-position dependence, we individually excite and measure all eight sublattice sites within the unit cell indexed by (5,5,5) in the 3D sample. For each excitation, the modal weights are calculated using the same projection procedure, and the final weights are obtained by averaging over all eight excitation configurations. This averaging procedure ensures that all eigenmodes are sufficiently sampled and eliminates the excitation selectivity associated with specific sites. The experimentally averaged results show that all four weights remain finite and are approximately equal at the degenerate frequency and wavevector, demonstrating that the measured response is a coherent superposition of all eigenmodes within the fourfold-degenerate manifold (see Note 10 in the Supplementary Information). This provides direct experimental evidence supporting the fourfold degeneracy of the self-dual band.

Data availability

All the data supporting the findings of this study are provided in the Source Data file and

Supplementary Information. Any additional information can be obtained from corresponding authors upon request. Source Data file has been deposited in Figshare under accession code https://doi.org/10.6084/m9.figshare.30148669 [49].

References

[1] Hou, J.-M. Hidden-symmetry-protected topological semimetals on a square lattice. *Phys. Rev. Lett.* **111**, 130403 (2013).

[2] Cariglia, M. Hidden symmetries of dynamics in classical and quantum physics. *Rev. Mod. Phys.* **86**, 1283 (2014).

[3] Po, H. C., Vishwanath, A. & Watanabe, H. Symmetry-based indicators of band topology in the 230 space groups. *Nat. Commun.* **8**, 50 (2017).

[4] Liu, Z. & Tegmark, M. Machine learning hidden symmetries. *Phys. Rev. Lett.* **128**, 180201 (2022).

[5] Witten, E. Duality, Spacetime and quantum mechanics. *Phys. Today* **50**, 28 (1997).

[6] Savit, R. Duality in field theory and statistical systems. *Rev. Mod. Phys.* **52**, 453 (1980).

[7] Maldacena, J. The large-N limit of superconformal field theories and supergravity. *Int. J. Theor. Phys.* **38**, 1113 (1999).

[8] Chen, J. *et al*. AdS/CFT correspondence in hyperbolic lattices, arXiv: 2305.04862 (2023).

[9] Wegner, F. J. Duality in generalized Ising models and phase transitions without local order parameters. *J. Math. Phys.* **12**, 2259 (1971).

[10] Hsieh, C.-T., Tachikawa, Y. & Yonekura, K. Anomaly of the electromagnetic duality of Maxwell theory. *Phys. Rev. Lett.* **123**, 161601 (2019).

[11] Khanikaev, A. B. *et al.* Photonic topological insulators. *Nat. Mater.* **12**, 233 (2013).

[12] Zhang, Q. *et al.* General duality and magnet-free passive phononic Chern insulators. *Nat. Commun.* **14**, 916 (2023).

[13] Chen, H., Chan, C. T. & Sheng, P. Transformation optics and metamaterials. *Nat. Mater.* **9**, 387 (2010).

[14] Fernandez-Corbaton, I. & Molina-Terriza, G. Role of duality symmetry in transformation optics. *Phys. Rev. B* **88**, 085111 (2013).

[15] Xu, L. & Chen, H. Conformal transformation optics. *Nat. Photonics* **9**, 15 (2015).

[16] Fruchart, M. & Vitelli, V. Symmetries and dualities in the theory of elasticity. *Phys. Rev. Lett.* **124**, 248001 (2020).

[17] Fruchart, M., Zhou, Y. & Vitelli, V. Dualities and non-Abelian mechanics. *Nature* **577**, 636 (2020).

[18] Danawe, H., Li, H., Ba'ba'a, H. A. & Tol, S. Existence of corner modes in elastic twisted Kagome lattices. *Phys. Rev. B* **104**, L241107 (2021).

[19] Lei, Q.-L. *et al.* Duality, hidden symmetry, and dynamic isomerism in 2D hinge structures. *Phys. Rev. Lett.* **129**, 125501 (2022).

[20] Allein, F. *et al.* Strain topological metamaterials and revealing hidden topology in higher-order coordinates. *Nat. Commun.* **14**, 6633 (2023).

[21] Azizi, P., Sarkar, S., Sun, K. & Gonella, S. Dynamics of self-dual kagome metamaterials and the emergence of fragile topology. *Phys. Rev. Lett.* **130**, 156101 (2023).

[22] Chen, Z. Y., Zhang, Z., Yang, S. A. & Zhao, Y. X. Classification of time-reversal-invariant crystals with gauge structures. *Nat. Commun.* **14**, 743 (2023).

[23] Benalcazar, W. A., Bernevig, B. A. & Hughes, T. L. Quantized electric multipole insulators. *Science* **357**, 61 (2017).

[24] Qi, Y. *et al.* Acoustic realization of quadrupole topological insulators. *Phys. Rev. Lett.* **124**, 206601 (2020).

[25] Xue, H. *et al.* Observation of an acoustic octupole topological insulator. *Nat. Commun.* **11**, 2442 (2020).

[26] Ni, X. *et al.* Demonstration of a quantized acoustic octupole topological insulator. *Nat. Commun.* **11**, 2108 (2020).

[27] Rui, W. B., Zhao, Y. X. & Wang, Z. D. Making topologically trivial non-Hermitian systems nontrivial via gauge fields. P*hys. Rev. Lett*. **131**, 176402 (2023).

[28] Han, Y.-H. *et al.* Observation of gauge field induced non-Hermitian helical skin effects, Chin. Phys. Lett. 10.1088/0256-307x/43/4/040704 (2026).

[29] Zhao, Y. X., Chen, C., Sheng, X.-L. & Yang, S. A. Switching spinless and spinful topological phases with projective PT symmetry. *Phys. Rev. Lett.* **126**, 196402 (2021).

[30] Meng, Y. *et al*. Spinful topological phases in acoustic crystals with projective *PT* symmetry. *Phys. Rev. Lett.* **130**, 026101 (2023).

[31] Zhao, Y. X., Huang, Y.-X. & Yang, S. A. Z_2-projective translational symmetry protected topological phases. *Phys. Rev. B* **102**, 161117 (2020).

[32] Li, T. *et al*. Acoustic Möbius insulators from projective symmetry. *Phys. Rev. Lett.* **128**,

116803 (2022).
[33] Xue, H. *et al*. Projectively enriched symmetry and topology in acoustic crystals. *Phys. Rev. Lett.* **128**, 116802 (2022).
[34] Chen, Z. Y., Yang, S. A. & Zhao Y. X. Brillouin Klein bottle from artificial gauge fields. *Nat. Commun.* **13**, 2215 (2022).
[35] Pu, Z. *et al*. Acoustic Klein bottle insulator. *Phys. Rev. B* **108**, L220101 (2023).
[36] Zhu, Z. *et al*. Brillouin Klein space and half-turn space in three-dimensional acoustic crystals. *Sci. Bull.* **69**, 2050-2058 (2024).
[37] Gao, F. *et al*. Orbital topological edge states and phase transitions in one-dimensional acoustic resonator chains. *Nat. Commun.* **14**, 8162 (2023).
[38] Fruchart, M., Yao, C. & Vitelli, V. Systematic generation of Hamiltonian families with dualities. *Phys. Rev. Research* **5**, 023099 (2023).
[39] Judson, T. W. Abstract algebra: theory and applications, *Virginia Commonwealth University Mathematics*, (2020).
[40] Di Liberto, M., Goldman, N. & Palumbo, G. Non-Abelian Bloch oscillations in higher-order topological insulators. *Nat. Commun.* **11**, 5942 (2020).
[41] Caselle, M., Gliozzi, F., Magnea, U. & Vinti, S. Width of long colour flux tubes in lattice gauge systems. *Nucl. Phys. B* **460**, 397 (1996).
[42] Pan, N., Chen, T., Ji, T., Tong, X. & Zhang, X. Three-dimensional non-Abelian Bloch oscillations and higher-order topological states. *Commun. Phys.* **6**, 355 (2023).
[43] Wieder, B. J., Kim, Y., Rappe, A. M. & Kane, C. L. Dirac semimetals in three dimensions. *Phys. Rev. Lett.* **116**, 186402 (2016).
[44] Rotman, J. An introduction to the theory of groups. 4th edition, *Springer, New York, USA*, (1994).
[45] Deng, Y., Benalcazar, W. A., Chen, Z. G., Oudich, M., Ma, G. & Jing, Y., Observation of degenerate zero-energy topological states at disclinations in an acoustic lattice. *Phys. Rev. Lett.* **128**, 174301 (2022).
[46] Mercadé, L., Pelka, K., Burgwal, R., Xuereb, A., Martínez, A. & Verhagen, E., Floquet phonon lasing in multimode optomechanical systems. *Phys. Rev. Lett.* **127**, 073601 (2021).
[47] Dong, X. L., Li, P. B., Liu, T. & Nori, F., Unconventional quantum sound-matter interactions in spin-optomechanical-crystal hybrid systems. *Phys. Rev. Lett.* **126**, 203601 (2021).

[48] Landi, M., Zhao, J., Prather, W. E., Wu, Y. & Zhang, L., Acoustic Purcell effect for enhanced emission. *Phys. Rev. Lett.* **120**, 114301 (2018).

[49] Meng Y. *et al*, Gauge-field-induced duality group in metamaterials, Figshare, https://doi.org/10.6084/m9.figshare.30148669, (2026).

Funding

Z.G. discloses support for the research of this work from the National Key R&D Program of China [grant number 2025YFA1412300], the National Natural Science Foundation of China [grant numbers 62375118 and 62361166627], the Guangdong Basic and Applied Basic Research Foundation [grant number 2024A1515012770], the Shenzhen Science and Technology Innovation Commission [grant number 20230802205352003], and High-level Special Funds [grant number G03034K004]. Y.M. discloses support for the research of this work from the National Natural Science Foundation of China [grant number 12304484] and the Guangdong Basic and Applied Basic Research Foundation [grant number 2024A1515011371]. Y.H.Y. discloses support for the research of this work from the National Natural Science Foundation of China [grant number 62175215] and the Fundamental Research Funds for the Central Universities [grant number 2021FZZX001-19]. H.X.S. discloses support for the research of this work from the National Natural Science Foundation of China [grant numbers 12274183 and 12174159], the Jiangsu Qing Lan Project, and the National Key Research and Development Program of China [grant number 2020YFC1512403]. Z.X.Z. discloses support for the research of this work from the National Natural Science Foundation of China [grant number 12404053] and the Guangdong Basic and Applied Basic Research Foundation [grant number 2025A1515012284]. Q.H.L. discloses support for the research of this work from the National Natural Science Foundation of China [grant number 12525410] and the Shenzhen Science and Technology Program [grant numbers RCJC20221008092722009 and 20231117091158001]. X.X. discloses support for the research of this work from the National Natural Science Foundation of China [grant number 62405053] and the Basic and Applied Basic Research Foundation of Guangdong Province [grant number 2025A1515012229].

Authors Contributions

Z.G. and Y.M. initiated the project. Y.M., Z.X.Z., and L.Y.Y. performed the simulations. Q.H.L., N.F.Z., Z.G., and Y.M. conducted the group theory analysis. Y.M., Z.X.Z., and Z.G. designed the experiments. X.X., B.Y., Z.X.Z., J.M.C., and Y.M. fabricated samples. H.X.S., H.Y.Z., Y.G., Y.J.G., and S.Q.Y. carried out the measurements. Y.M., Z.G., Q.H.L., and Y.H.Y. analyzed the data. Y.M., Z.G., Y.H.Y., N.F.Z., Q.H.L., R.Y.Z., G.G.L., C.S., and H.S.C. wrote the manuscript. Z.G., Y.M., Y.H.Y., and Q.H.L. revised the manuscript. All authors discussed the results and contributed to the final version of the manuscript. Z.G., Y.H.Y., Q.H.L., S.Q.Y., and Y.M.

supervised the project.

Competing interests

The authors declare no competing interests.

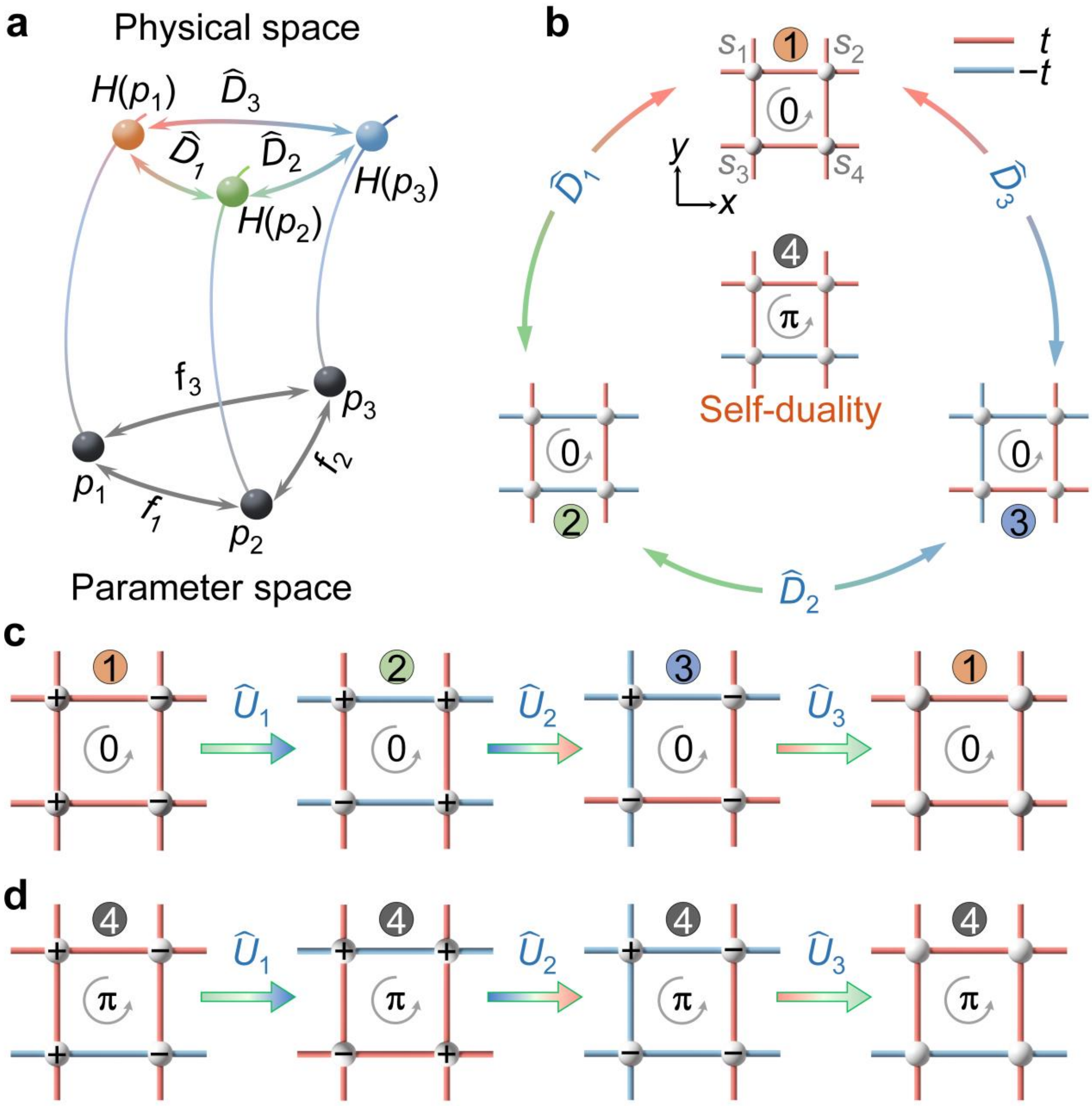

Fig. 1 | Multi-to-multi mappings between duality groups in 2D systems. a, Dualities between Hamiltonian groups $H(p_i)$ in the physical space (blue region), where p_i in the parameter space (gray region) can be transformed by the function f_i. The Hamiltonian groups $H(p_i)$ can be mapped onto each other by dual operators $\widehat{D}_i$. **b**, Schematic illustration of duality transformations (curved arrows, $\widehat{D}_i$) between dual lattices (①, ②, ③) and self-dual lattice (④) in 2D system. 0 and π denote the gauge flux. Gray spheres represent the sites indexed by s_m; red (blue) bonds represent the positive (negative) hoppings. **c**, Gauge transformation between duality lattices within a duality group. **d**, Invariance of the self-dual lattice under all gauge transformation operators.

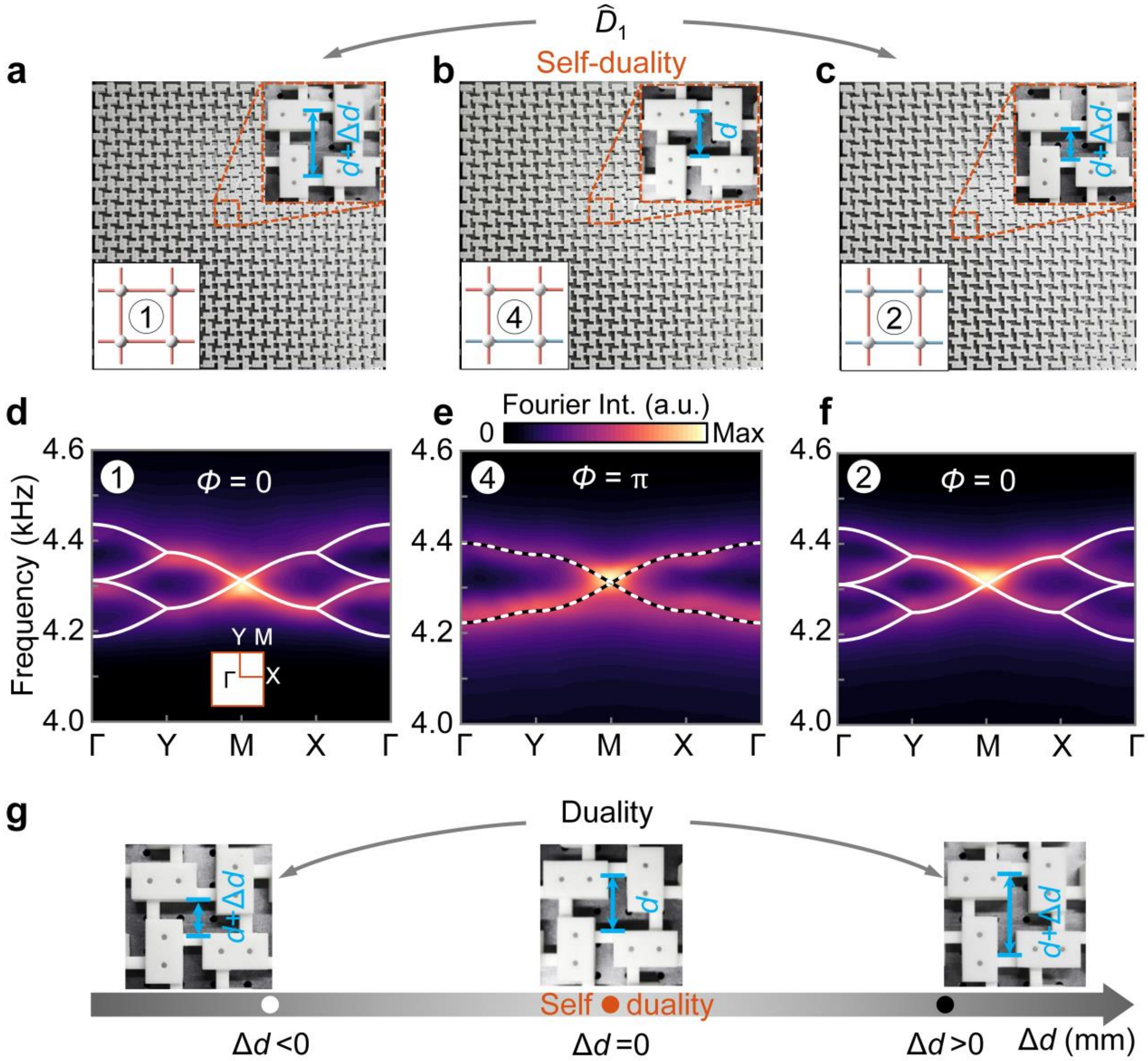

Fig. 2 | Experimental demonstration of the duality group and self-duality in 2D acoustic metamaterials. a-c, Photographs of the 2D acoustic metamaterials of two duality systems (**a**) and (**c**) and a self-duality system (**b**). The red-dashed rectangles mark the unit cells, with their details enlarged in the upper-right insets. All samples are characterized by a geometrical parameter Δd: for lattice ① $\Delta d > 0$, for lattice ② $\Delta d < 0$, and for lattice ④ $\Delta d = 0$ (upper right insets), respectively. **d-f**, Measured (color maps) and calculated (white and black lines) band structures of two duality acoustic metamaterials with identical band structure (**d** and **f**) and the self-duality acoustic metamaterial with Kramers-like double-degenerate band structure across the entire 2D BZ (**e**). Inset in (**d**) is the first 2D BZ of the square lattice. **g**, Schematic illustration of the duality relation between acoustic metamaterial samples with $\Delta d > 0$ and $\Delta d < 0$, and the self-duality point at $\Delta d = 0$.

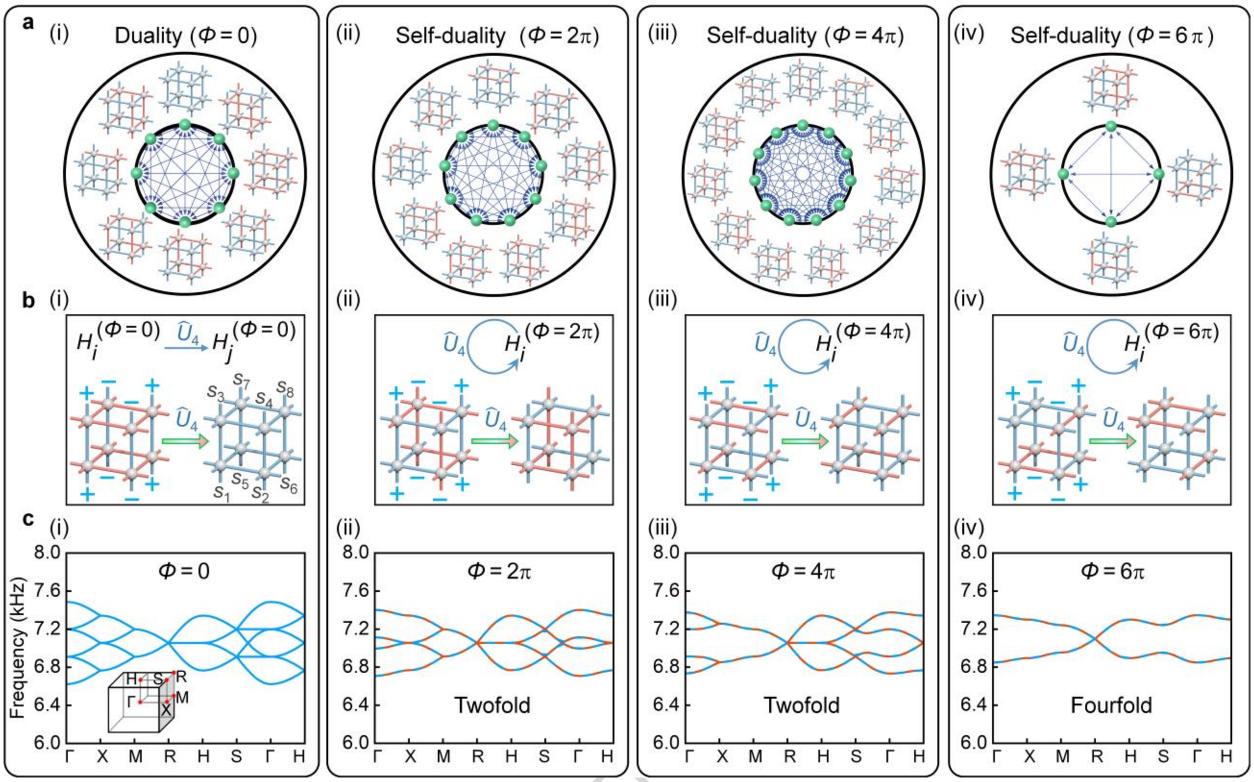

Fig. 3 | Multi-to-multi mappings within duality groups and self-duality groups in 3D systems. **a**, (i) Eight inequivalent dual lattices with 0-gauge flux. (ii)-(iii) The self-duality group comprises nine (eleven) lattices with 2π-gauge flux (4π-gauge flux). (iv) The self-duality group comprises four lattices with 6π-gauge flux. **b**, (i) Gauge transformation between two duality lattices in the duality group with 0-gauge flux via the operator $\widehat{U}_4$. (ii)-(iv) The invariance of self-duality lattices under the $\widehat{U}_4$ operator in the self-duality group with 2π, 4π, and 6π-gauge flux, respectively. **c**, (i)-(iv) Calculated bulk band structures of duality lattices with 0-gauge flux **c**(i) and self-duality lattices with 2π **c**(ii), 4π **c**(iii), and 6π **c**(iv) gauge flux, respectively. The inset in **c**(i) shows the 3D BZ of the cubic lattice. Red (blue) bonds represent positive (negative) couplings.

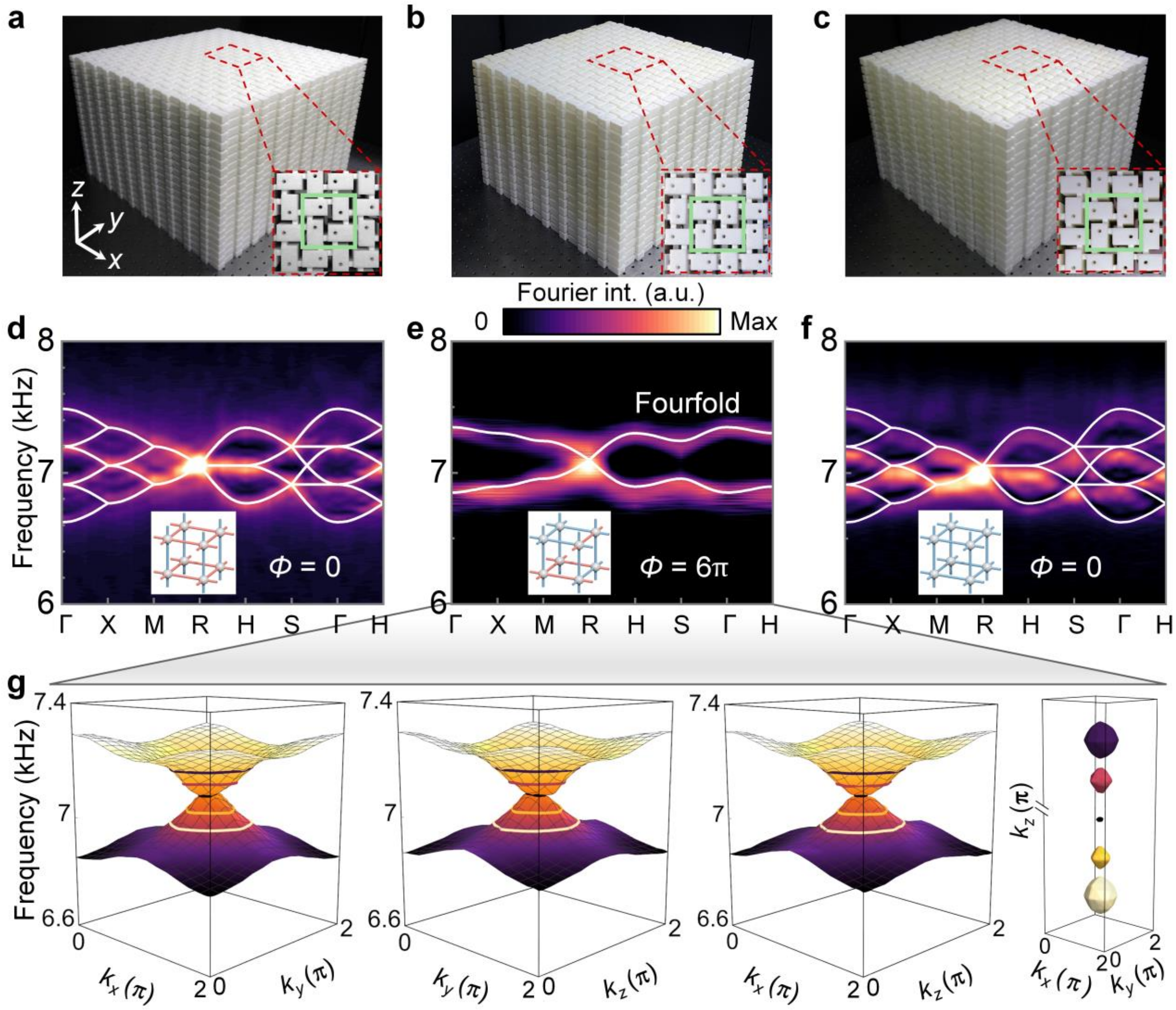

Fig. 4 | Experimental demonstration of the duality group and self-duality group in 3D acoustic metamaterials. a-c, Photographs of the fabricated 3D acoustic metamaterials, two duality samples (**a**) and (**c**), and one self-duality sample (**b**). Insets: zoomed-in of selected regions (red dashed rectangle), with green rectangles indicating top view of the unit cells. **d-f**, Measured (color maps) and calculated (white lines) band structures of the 3D acoustic metamaterials in (**a**)-(**c**). Insets: corresponding 3D tight-binding configurations. **g**, Measured 3D band structures and iso-frequency contour surfaces of the eightfold degenerate 3D double Dirac point in **k**-space.

Editorial Summary

Research on dualities is commonly restricted to one-to-one mappings. Here, by incorporating artificial gauge fields, the authors demonstrate 2D and 3D acoustic metamaterials enabling $\mathbb{Z}_2 \times \mathbb{Z}_2$ and $(\mathbb{Z}_2)^6$ duality groups, respectively, where distinct structures share identical band structures, and self-duality gives rise to symmetry-protected high-order degeneracies.

Peer review information: *Nature Communications* thanks Yosuke Nakata and the other, anonymous, reviewers for their contribution to the peer review of this work. A peer review file is available.